

Evolution of stars with 60 and 200 M_{\odot} : predictions for WNh stars in the Milky Way.

A. C. Gormaz-Matamala^{1,2}, A. Romagnolo¹, and K. Belczynski^{1*}

¹ Nicolaus Copernicus Astronomical Center, Polish Academy of Sciences, Bartycka 18, 00-716 Warsaw, Poland

² Astronomický ústav, Akademie věd České republiky, Fričova 298, 251 65 Ondřejov, Czech Republic
e-mail: alex.gormaz@uv.c1

ABSTRACT

Context. Massive stars are characterised by powerful stellar winds driven by radiation, and therefore mass-loss rate plays a crucial role in their evolution.

Aims. We study in detail the evolution of two massive stars (a classical massive star and a very massive star) at solar metallicity ($Z = 0.014$) taken from Romagnolo et al. (2024, Paper I); by calculating their final masses, radial expansion, and chemical enrichment, at their H-core, He-core and C-core burning stages prior to the final collapse.

Methods. We run evolutionary models for initial masses 60 and 200 M_{\odot} , using MESA and the Geneva-evolution-code (GENEC). For the mass loss, we adopt the self-consistent m-CAK prescription for the optically thin winds of OB-type stars, a semi-empirical formula for H-rich optically thick wind of WNh stars, and a hydrodynamically consistent formula for the H-poor thick wind of classical Wolf-Rayet stars. For both evolution codes, we set initial rotation as 40% of the critical angular velocity, overshooting $\alpha_{\text{ov}} = 0.5$, Tayler-Spruit for the angular momentum transport, and Ledoux criterion for the treatment of convective layers.

Results. As seen from Paper I, the unification of the initial setup for stellar structure and wind prescription leads into very similar M_{bh} for both GENEC and MESA codes. However, both codes predict different tracks across the HRD. For the 60 M_{\odot} case, GENEC models predict a more efficient rotational mixing and more chemically homogeneous evolution, whereas MESA model predicts a large radial expansion post-MS reaching the LBV phase. For the 200 M_{\odot} case, differences between both evolution codes are less relevant because their evolution is dominated by wind mass loss with a weaker dependence on internal mixing, and only the selected treatment for superadiabacity creates an impact during the He-burning stage.

Conclusions. The switch of the mass-loss prescription based on the proximity to the Eddington factor instead of the removal of outer layers, implies the existence of WNh stars with a large mass fraction of hydrogen at the surface ($X_{\text{surf}} \geq 0.3$) formed from initial masses of $\geq 60 M_{\odot}$. These stars are constrained in a T_{eff} range of the HRD which corresponds to the MS band, in agreement with the observations of Galactic WNh stars at $Z = 0.014$. While our models employ a fixed $\Gamma_{\text{e,trans}}$ threshold for the switch to thick winds, rather than a continuous thin-to-thick wind model, the good reproduction of observations supports the robustness of the wind model upgrades introduced in Paper I, allowing its application to studies of late-stage stellar evolution before core collapse.

Key words. Stars: early-type – Stars: evolution – Stars: mass-loss – Stars: winds, outflows – Stars: Wolf-Rayet

1. Introduction

The detection of the first source of gravitational waves (GW, Abbott et al. 2016, 2021) opened the door for a large number of studies dedicated to find more GW sources in the Universe, namely *double compact objects* (hereafter DCO) mergers. Rates of these DCO merger events depend on considered conditions for the binary system concerning the orbital separation, the formation (or not) of a common envelope (CE), as well as the initial assumptions for RLOF and their timescales (Ivanova et al. 2013; Olejak et al. 2021). Moreover, these modes are intimately linked with the single evolution of the stars in a binary system, which is crucial to determine the final remnant masses (Belczynski et al. 2010; Bavera et al. 2023; Romagnolo et al. 2024) and the maximum radial expansion that the stellar components can reach during their evolution (Agrawal et al. 2020; Romagnolo et al. 2023), reason why accurate evolution models are necessary to constrain the theoretical rate of the DCO merging events.

Stellar black holes are the final fate of massive stars with $M_{\text{zams}} \gtrsim 25 M_{\odot}$ (Heger et al. 2003). Even though the condi-

tions of the death as supernovae also constrain the mass of the final remnant (Fryer et al. 2022; Olejak et al. 2022), the stellar mass prior to the supernova explosion is explicitly dependent of the mass-loss rate (denoted as dM/dt or simply \dot{M}) carried out by the strong winds during the evolution of a massive stars (Vink 2021). Because stellar winds of massive stars are driven by line-force (Lucy & Solomon 1970; Castor et al. 1975; Abbott 1982), these \dot{M} are directly dependent on metallicity. This explains the predominance of more massive black holes in less metallic environments (Farrell et al. 2021; Vink et al. 2021), although exceptions due to unusually weaker winds can also be theoretically described (Belczynski et al. 2020a). Moreover, the strength of the stellar winds varies along the evolution of the star, which is dominated during the main sequence (H-core burning stage) by line-driven optically thin winds for OB-type stars (Puls et al. 2008), then eventual strong outflows might stem during the LBV stage (Humphreys et al. 2016), and finally we find optically thick winds of Wolf-Rayet (WR) stars for the more evolved stages (Crowther 2007; Gräfener & Hamann 2008). Optically thick winds are naturally denser, and therefore the mass loss during the WR phase is higher in comparison with OB-type phase.

* Deceased on 13th January 2024.

Recent theoretical (Krtićka & Kubát 2017, 2018; Gormaz-Matamala et al. 2019, 2022a; Björklund et al. 2021) and empirical studies (Hawcroft et al. 2021, 2024) have found theoretical values for the \dot{M} of massive stars to be in the order of ~ 3 times lower than the standard mass-loss recipe from Vink et al. (2001, hereafter V01). Such difference in the value of mass loss is enough to alter the evolution of stars with $M_{\text{zams}} \gtrsim 20 M_{\odot}$ (Meynet et al. 1994). Adopting new winds, massive stars will retain more mass during their main sequence phase, thus being larger and more luminous (Gormaz-Matamala et al. 2022b; Björklund et al. 2023). Besides, massive stars keep larger rotational velocities for a more extended time, because they lose less angular momentum (Gormaz-Matamala et al. 2023). Even though these changes in the stellar evolution have been applied mostly for the early H-burning stages, they also impact the further evolution of the subsequent stages (Gormaz-Matamala et al. 2024; Josiek et al. 2024). Moreover, considering that also the mass-loss prescription for WR winds has been revisited (Bestenlehner 2020; Sander & Vink 2020) as well as its impact on the stellar evolution (Higgins et al. 2021), the entire panorama of the stellar evolution is being upgraded.

In Romagnolo et al. (2024, hereafter Paper I), we calculate the remnant mass for a set of initial masses from 10 to $300 M_{\odot}$ for $Z = 0.014$, based on stellar evolution models adopting the state-of-the-art physical ingredients such as Tayler-Spruit dynamo, larger core-convective overshooting, and new mass-loss recipes. As a result, we found a maximum black hole mass of $M_{\text{bh,max}} = 28.3 M_{\odot}$ formed from stars with $M_{\text{zams}} \gtrsim 250 M_{\odot}$, larger than the previous $M_{\text{bh,max}} \approx 20 M_{\odot}$ from Belczynski et al. (2010) but quite below the maximum BH masses predicted by Bavera et al. (2023, $\approx 35 M_{\odot}$ at $M_{\text{zams}} = 75 M_{\odot}$) and (Martinet et al. 2023, $\approx 42 M_{\odot}$ at $M_{\text{zams}} = 180 M_{\odot}$). Even though the recently discovered largest BH in the Milky Way has a mass of $M_{\text{bh,max}} = 32.7 \pm 0.70 M_{\odot}$ (Gaia Collaboration et al. 2024), the low metallicity of its star companion suggest that this black hole was formed from a metal poor massive star and thus our predicted $M_{\text{bh,max}}$ remains valid.

Moreover, the new wind prescription introduced in Paper I entail more implications concerning the evolution of massive stars. Standard evolution models (Ekström et al. 2012; Choi et al. 2016) adopted the switch from OB-type to WR-type winds once the stellar surface removes the majority of its hydrogen. Nevertheless, theoretical studies have found that the transition from optically thin to thick winds during the evolution of massive stars is more due to the proximity to the Eddington limit rather than due to the removal of the outer envelopes (Vink et al. 2011; Gräfener et al. 2011), thus altering the expected lifetimes and total amount of mass removed at each evolutionary stage. Because of this, in Paper I we set the switch between optically thin to optically thick winds according to the proximity to the Eddington limit instead of based on the chemical composition of the stellar outer envelope. As a consequence, the most massive stars develop thick winds already during their earliest evolution stages, altering their tracks over the HR diagram and predicting the existence of WR stars with hydrogen abundance $X_{\text{surf}} \geq 0.3$ in their surfaces, the so-called WNh stars (Martins et al. 2008; Crowther et al. 2010).

In this work, we study in detail the impact of the already mentioned upgrades on the evolution of two stars from Paper I, with special emphasis on the existence of H-rich WR stars. For that purpose, we run evolution models for the stars with initial masses of 60 and $200 M_{\odot}$ at solar metallicity ($Z = 0.014$), following Asplund et al. (2009). We introduce our mass-loss prescription in Sec. 2.2, together with the description of the switch

from optically thin to thick winds at $\Gamma_e = 0.5$. The resulting evolution tracks over the HR diagram for our models are detailed in Sec. 3, whereas the observational diagnostics comparing with spectroscopic analyses are shown in Sec. 4. Finally, conclusions are summarised in Sec. 5.

2. Ingredients for stellar evolution models

2.1. Stellar evolution codes

Same as in Paper I, we perform our stellar evolution models using the codes MESA (Modules for Experiments in Stellar Astrophysics, Paxton et al. 2011, 2013, 2015, 2018, 2019; Jermyn et al. 2023) and the Geneva-evolution-code (Eggenberger et al. 2008, hereafter GENEC). For step-overshooting, we adopt a value for α_{ov} of 0.5, in agreement with the most recent studies on convective cores (Martinet et al. 2021; Scott et al. 2021; Baraffe et al. 2023). Concerning angular momentum transport, we include for both MESA and GENEC codes the Tayler-Spruit dynamo (Tayler 1973; Spruit 2002; Heger et al. 2005), whereas we replace the treatment for the convective layers from Schwarzschild to Ledoux’s criterion (Ledoux 1947). For a more detailed explanation about our treatment for the stellar interior, see Romagnolo et al. (2024, Sec. 2).

2.2. Mass loss for massive and very massive stars

Evolutionary tracks of massive stars adopting lower \dot{M} are in rule with the observed mass loss of clumped winds (Bouret et al. 2005; Muijres et al. 2011; Šurlan et al. 2013), as well as with more detailed calculations for the wind structure of O-type stars by self-consistently solving radiative transfer equations at full NLTE conditions (Sander et al. 2017; Sundqvist et al. 2019; Gormaz-Matamala et al. 2021). However, this scenario can hardly be extended to higher masses such as VMS, whose mass-loss rates values even larger than the given ones by V01 (Vink et al. 2011). Their stellar winds are so strong that they develop WR-type spectral profile with broad emission lines before the end of the H-core burning stage (WNh stars). The limit between VMS and “regular” massive stars is normally set around $M_{\text{zams}} \sim 100 M_{\odot}$, although this value may vary by means of rotation, metallicity, and specially mass-loss input (Yusof et al. 2013; Köhler et al. 2015).

Evolution of VMS, revisiting the transition between formal O-type to WNh stars, has been just recently analysed by Gräfener (2021) and Sabhahit et al. (2023). Despite this, standard evolution codes still assume the transition of the wind regime based on the surface composition (when the hydrogen mass fraction becomes $X_{\text{surf}} \leq 0.3$ for GENEC and $X_{\text{surf}} \leq 0.4$ for MESA) the mass-loss recipe switches from the prescription for optically thin V01 to optically thick winds according to Gräfener & Hamann (2008, hereafter GH08¹). However, spectroscopic diagnostics have found WNh spectral features for VMS with surface hydrogen abundances as high as $X_{\text{surf}} \approx 0.7$ in the Milky Way (Martins 2023) and in the Large Magellanic Cloud (Tehrani et al. 2019; Martins & Palacios 2022), thus strengthening the idea that the transition to thick winds should be based on another criteria apart from surface chemical composition.

¹ Nevertheless, evolution models used to both V01 and GH08 to describe mass loss from WR winds, depending on which recipe provided the largest \dot{M} at certain point (Yusof et al. 2013).

2.2.1. Winds in the proximity to the Eddington limit

There is evidence that the change in the mass-loss regime for VMS from O-type optically thin winds to WR optically thick winds is not because of the chemical composition at the surface, but because of the proximity to the Eddington limit (Gräfener et al. 2011), with the Eddington factor defined as the ratio between the total radiative and the gravitational acceleration in the stellar structure.

$$\Gamma_{\text{Edd}}(r) = \frac{g_{\text{rad}}}{g_{\text{grav}}} = \frac{\kappa(r)L(r)}{4\pi cGM(r)}, \quad (1)$$

with $\kappa(r)$ being the total flux-mean opacity of all the radiative processes. Because of its radial dependence, Γ_{Edd} adopts different values across the stellar structure from below the photosphere to the wind, hence it does not provide a single value to evaluate the proximity to the Eddington limit. Instead, given that the atmosphere of hot stars is expected to be totally ionised, we can evaluate the proximity to the Eddington limit of the entire star by means of the *classical* Eddington factor, which considers only the electron scattering for the radiative processes, Γ_e

$$\Gamma_e = \frac{g_e}{g_{\text{grav}}} = \frac{L_* \kappa_e}{4\pi cGM_*}, \quad (2)$$

with κ_e being the electron scattering opacity. For simplicity, Eddington factor is usually expressed as a function of stellar mass, luminosity and hydrogen abundance

$$\log \Gamma_e = -4.813 + \log(1 + X_{\text{surf}}) + \log(L/L_{\odot}) - \log(M/M_{\odot}). \quad (3)$$

The star is hydrostatically stable if $\Gamma_e < 1$, i.e., if the acceleration due to radiative processes is smaller than gravity, otherwise the star would disrupt itself. And yet the effects of radiation ‘peeling off’ the star can be observed below such threshold. If $\Gamma_{\text{Edd}}(r)$ is locally larger than 1 at some layers, these layers will be subject to a physical phenomenon called *envelope inflation*, which leads to an inversion in the density profile $\rho(r)$ equivalent to an expansion of the hydrostatic stellar radius (Ishii et al. 1999; Petrovic et al. 2006). Envelope inflation is thought to be linked with the radius problem of the WR stars (Meynet & Maeder 2005) or with the instabilities of the LBV phenomenon, once it is satisfied that $\Gamma_e \gtrsim 0.3 - 0.35$ (Gräfener et al. 2012).

Moreover, mass loss of VMS is directly dependent on the Eddington factor, and the relationship quickly escalates when the Eddington limit is approached (Vink et al. 2011; Vink & Gräfener 2012). Numerical models found a kink in the slope of the $\dot{M} \propto \Gamma_e$ dependence at $\Gamma_e \approx 0.7$, after the which the mass-loss scales with the Eddington factor in agreement with the relationship found for Gräfener & Hamann (2008) for WR stars. Posteriori observational diagnostics on very massive stars found that wind clumping and uncertainties affects the accuracy to determine the transition Γ_e , which can be set as low as Γ_e as low as ≈ 0.3 (Bestenlehner et al. 2014). A more theoretically detailed study is provided by Sabhahit et al. (2023), where the Γ_e to switch the wind regime is directly correlated with the wind efficiency at different metallicities. However, the existence of this kink in the $\dot{M} \propto \Gamma_e$ dependance, ensuring a smooth transition (i.e., without any abrupt jump) between optically thin and thick wind regimes, still considers V01 recipe for low Γ_e . Such smoothness seems to be more related with the enhanced values for mass loss given by V01, which can calculate \dot{M} values higher than GH08 for the upper part of HRD (see footnote 1).

Instead, we aim for a transition point between the most updated thin winds (Krtićka & Kubát 2017; Björklund et al. 2021;

Gormaz-Matamala et al. 2022b) and thick winds. For this, we based our transition in the upper limit of validity of our m-CAK prescription (Gormaz-Matamala et al. 2019). Bestenlehner (2020) extended the theoretical calculation of \dot{M} according to the CAK theory (Castor et al. 1975) for regimes closer to the Eddington limit, finding also a transition $\Gamma_{e,\text{trans}}$ beyond the which the slope of the relation $\dot{M} \propto \Gamma_e$ become steeper as the observations from Bestenlehner et al. (2014). This $\Gamma_{e,\text{trans}}$ ranges from ~ 0.46 to ~ 0.48 , depending on the value of the CAK line-force parameter² α . For $\alpha \sim 0.4 - 0.6$, which are the values found from the self-consistent line-force parameters found by Gormaz-Matamala et al. (2022b) for stars with masses in the range of 25 to 120 M_{\odot} and metallicities from $Z = 0.014$ (solar) to $= 0.002$ (SMC), the value of the transition Eddington factor keeps relatively constant around $\Gamma_{e,\text{trans}} \approx 0.48$. Therefore, given that our new prescription for optically thin winds is based on the m-CAK theory, we establish $\Gamma_e = 0.5$ as the transition point between thin and thick winds for our evolution models.

2.3. Mass-loss recipes for thin and thick winds

2.3.1. Mass loss for the H-core burning stage

For thin winds ($\Gamma_e \leq 0.5$), we use the mass-loss prescription from Gormaz-Matamala et al. (2022b, 2023)

$$\begin{aligned} \log \dot{M}_{\text{thin}} = & -40.314 + 15.438 w + 45.838 x - 8.284 w x \\ & + 1.0564 y - w y / 2.36 - 1.1967 x y \\ & + z \times \left[0.4 + \frac{15.75}{M_*/M_{\odot}} \right], \end{aligned} \quad (4)$$

where \dot{M}_{thin} is in $M_{\odot} \text{ yr}^{-1}$; and where w , x , y , and z are defined as

$$w = \log\left(\frac{T_{\text{eff}}}{\text{kK}}\right), \quad x = \frac{1}{\log g}, \quad y = \frac{R_*}{R_{\odot}}, \quad z = \log\left(\frac{Z_*}{Z_{\odot}}\right).$$

As mentioned in Gormaz-Matamala et al. (2023), the dependence between mass loss and metallicity is not constant but it intrinsically depends on the mass (and the luminosity), because the radiative acceleration for more massive and luminous stars is mostly dominated by the continuum over the line-acceleration (see also Krtićka & Kubát 2018).

The range of validity of Eq. 4 is for $T_{\text{eff}} \geq 30 \text{ kK}$ and $\log g \geq 3.2$. Beyond these values, we return to V01. For the cases when $T_{\text{eff}} \leq 10 \text{ kK}$, mass loss is described by de Jager et al. (1988).

For thick winds ($\Gamma_e > 0.5$), since we establish the transition from the theoretical analysis of Bestenlehner (2020), we use their $\dot{M}(\Gamma_e)$ recipe with the calibration performed by Brands et al. (2022)

$$\log \dot{M}_{\text{B22}} = -5.19 + 2.69 \log(\Gamma_e) - 3.19 \log(1 - \Gamma_e). \quad (5)$$

It is easy to see that, for $\Gamma_e = 0.5$ Eq. 5 becomes $\log \dot{M} \approx -5.04$. This value is very close of the ‘transition’ mass-loss rates empirically determined for the Arches and 30 Clusters by Sabhahit et al. (2023), i.e., the value for \dot{M} over the which the stars of the mentioned clusters exhibit a WNh spectrum. This implies that both approaches (Sabhahit et al. 2023, and this current study) find the transition between thin and thick winds at roughly the same mass-loss rate, although our prescription does

² Do not confuse this parameter α , which is one of the line-force parameters from CAK theory (Castor et al. 1975; Abbott 1982), with the α_{ov} for the convective core overshooting.

not require that transition to be smooth. Moreover, because this formula was calibrated for the VMS in the R136 star cluster at the LMC, with metallicity $Z = 0.006$ (Eggenberger et al. 2021), we add an extra term with the same metallicity dependence as for thin winds. Thus

$$\log \dot{M}_{\text{thick}} = \log \dot{M}_{\text{B22}} + \log \left(\frac{Z_*}{Z_{\text{LMC}}} \right) \times \left[0.4 + \frac{15.75}{M_*/M_\odot} \right], \quad (6)$$

Hence, despite we are using the same $\Gamma_{e,\text{trans}}$ for all metallicities, mass loss for optically thick winds incorporates a metallicity dependence which is consistent with the intrinsic dependence on mass/luminosity. Even though calibration from Brands et al. (2022) matches with the formula of Krtićka & Kubát (2018) (and subsequently with their intrinsic metallicity dependence on luminosity), we adopt the intrinsic metallicity dependence on mass introduced by Gormaz-Matamala et al. (2023) to keep coherence between our adopted thin and thick winds.

Analogous to Eq. 4 for thin winds, Eq. 6 is valid only for $T_{\text{eff}} \geq 30$ kK. For thick winds at cooler temperatures, we return to GH08 (Gräfener & Hamann 2008).

2.3.2. Mass loss for advanced evolutionary stages

The Eq. 6 from Bestenlehner (2020) and Brands et al. (2022) is valid for H-rich WR stars, either for the H-core or the He-core burning stages. Once the star has depleted the most part of its hydrogen ($X_{\text{surf}} \leq 10^{-7}$), the mass-loss rate follows the formula derived from the hydrodynamically consistent models for WR stars from Sander et al. (2020), whose final formula $\dot{M} \sim \Gamma_e$ is given by Sander & Vink (2020)

$$\log \dot{M} = a \log[-\log(1 - \Gamma_e)] - \log 2 \left(\frac{\Gamma_{e,d}}{\Gamma_e} \right)^{c_{d,b}} + \log \dot{M}_{\text{off}}, \quad (7)$$

where

$$\begin{aligned} a &= 2.932, \\ \Gamma_{e,b} &= -0.324 * \log \left(\frac{Z_*}{Z_\odot} \right) + 0.244, \\ c_{d,b} &= -0.44 * \log \left(\frac{Z_*}{Z_\odot} \right) + 9.15, \\ \log \dot{M}_{\text{off}} &= 0.23 * \log \left(\frac{Z_*}{Z_\odot} \right) - 2.61. \end{aligned}$$

We do not incorporate the latest improvements to this formula from Sander et al. (2023), because they add extra terms dependent on a quantity T_* which is not equivalent to the effective temperature T_{eff} , and thus such implementation is currently beyond the capacities of both codes MESA and GENEC. The only condition of validity for Eq. 7 is the criterion $X_{\text{surf}} \leq 10^{-7}$ (H-poor WR star), regardless of the Eddington factor of luminosity. Finally, we also mention that all the wind recipes considered here are thought for single stellar evolution, and for that reason we do not include wind recipes for peculiar scenarios coming from binary interaction, such as stripped low-mass helium stars (Vink 2017) or O-type stars with He-core burning (Pauli et al. 2022).

2.4. Treatment of rotation

The most important difference concerning rotation between MESA and GENEC is the standardisation. MESA sets stellar rotation as a fraction of the critical *angular* rotational velocity, ω ,

needed to disrupt the star due to centrifugal forces (Paxton et al. 2013), i.e.³

$$\Omega_{\text{MESA}} = \frac{\omega}{\omega_{\text{crit}}} \quad \text{with} \quad \omega_{\text{crit}}^2 = \frac{GM}{R^3} (1 - \Gamma_e). \quad (8)$$

On the other hand, GENEC sets stellar rotation as a fraction of the *linear* rotational velocity ($\Omega_{\text{GENEC}} = v/v_{\text{crit}}$). However, these two fractions are not equivalent because a rotating star loses its spherical shape and becomes oblate, thus meaning that the polar radius and the equatorial radius are not longer the same. This effect is not considered in MESA (Choi et al. 2016) but it is in GENEC, by means of the Roche-model (Ekström et al. 2008; Georgy et al. 2011). According to this, the ratios Ω_{MESA} and Ω_{Genec} are related as

$$\frac{v}{v_{\text{crit}}} = \left[\frac{\omega}{\omega_{\text{crit}}} 2 \left(\frac{R_{\text{eq}}}{R_{\text{pol}}} - 1 \right) \right]^{1/3}, \quad (9)$$

with R_{eq} and R_{pol} being the equatorial and the polar radii respectively. The standard setup has been $\Omega = 0.4$ (either $\omega/\omega_{\text{crit}}$ or v/v_{crit}), based on the survey on Galactic BSG performed by Huang et al. (2010). For the purpose of this paper, we set the initial rotation as $\Omega = \omega/\omega_{\text{crit}} = 0.4$ (equivalent to $v/v_{\text{crit}} \approx 0.276$).

The treatment of the stellar rotation also varies between both codes, not only for the mixing for also for the enhancement of the mass loss. MESA follows the standard correction factor from (Langer 1998)

$$\dot{M}(\omega) = \dot{M}(\omega = 0) \left(\frac{1}{1 - \omega/\omega_{\text{crit}}} \right)^{0.43}, \quad (10)$$

with ω the rotational angular velocity at the stellar equator, and ω_{crit} the break-up velocity needed to disrupt the star due to centrifugal forces. On the contrary, GENEC uses as correction factor the more complex formula provided by Maeder & Meynet (2000)

$$\dot{M}(\omega) = \dot{M}(0) \frac{(1 - \Gamma)^{\frac{1}{\alpha} - 1}}{\left[1 - \frac{\omega^2}{2\pi G \rho_m} - \Gamma \right]^{\frac{1}{\alpha} - 1}}, \quad (11)$$

with α the CAK line-force parameter, and Γ the Eddington factor. Eq. 11 considers the break-up velocity not only with respect to the rotation but also with respect to the proximity to the Eddington limit ($\Omega\Gamma$ -limit), together with being in rule with the so-called Ω -slow solutions (Curé 2004; Araya et al. 2018; Gormaz-Matamala et al. 2023).

3. Stellar evolution adopting new winds

3.1. H-core burning stage

Fig. 1 shows the evolutionary tracks across the HR diagram according to our new GENEC and MESA models, for both $60 M_\odot$ and $200 M_\odot$. Fig. 2 shows the evolution of the mass loss, the stellar mass, the stellar radius, and the rotational velocity, from the ZAMS until the end of the H-core burning stage.

We observe that, even though the ZAMS point in the HRD is almost the same for the MESA and GENEC tracks, MESA models start with a higher mass loss due to the more rigid effect

³ In this work, we denote Ω to the ratio between rotational velocity and critical velocity following the formalism of the line-driven theory (Curé & Rial 2004; Puls et al. 2008; Venero et al. 2024), whereas for the angular velocity we use the letter ω .

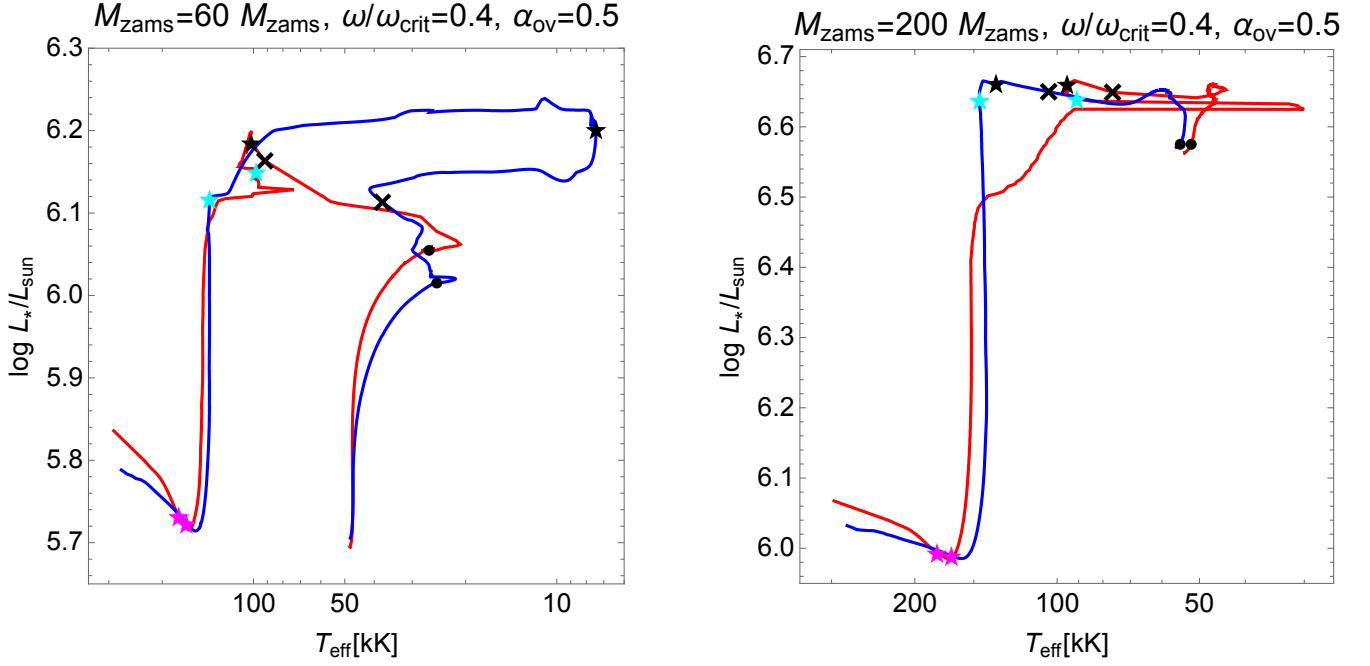


Fig. 1: HR diagram for GENEC (red) and MESA (blue) evolution models with 60 M_{\odot} (left panel) and 200 M_{\odot} (right panel). Black dots represent the point where $\Gamma_e = 0.5$ and thus the wind regime transits from thin to optically thick, black crosses represent the end of the H-core burning stage, black stars represent the beginning of the He-core burning stage, cyan stars represent the switch between H-rich to H-poor helium stars, and magenta stars represent the end of the He-core burning stage.

Table 1: Properties of our evolution models during the H-core burning stage.

Initial parameters		H-core burning												
M_{zams} [M_{\odot}]	code	τ_{switch} [Myr]	M_{switch} [M_{\odot}]	$X_{\text{surf,switch}}$	$Y_{\text{surf,switch}}$ mass fraction	$X(N)_{\text{surf,switch}}$	τ_{MS} [Myr]	M_{final} [M_{\odot}]	M_{core} [M_{\odot}]	R_{max} [R_{\odot}]	X_{surf}	Y_{surf} mass fraction	$X(N)_{\text{surf}}$	Γ_e
60	GENEC	3.959	53.6	0.514	0.472	0.008	4.284	42.1	33.6	82.6	0.057	0.929	0.008	0.562
60	MESA	3.734	51.9	0.632	0.354	0.007	4.186	44.5	37.2	73.1	0.417	0.569	0.009	0.605
200	GENEC	0.183	198.9	0.717	0.269	0.002	2.517	100.4	93.3	36.4	0.013	0.973	0.008	0.691
200	MESA	0.092	199.3	0.717	0.268	8×10^{-4}	2.543	100.7	100.7	23.6	0.021	0.966	0.009	0.696

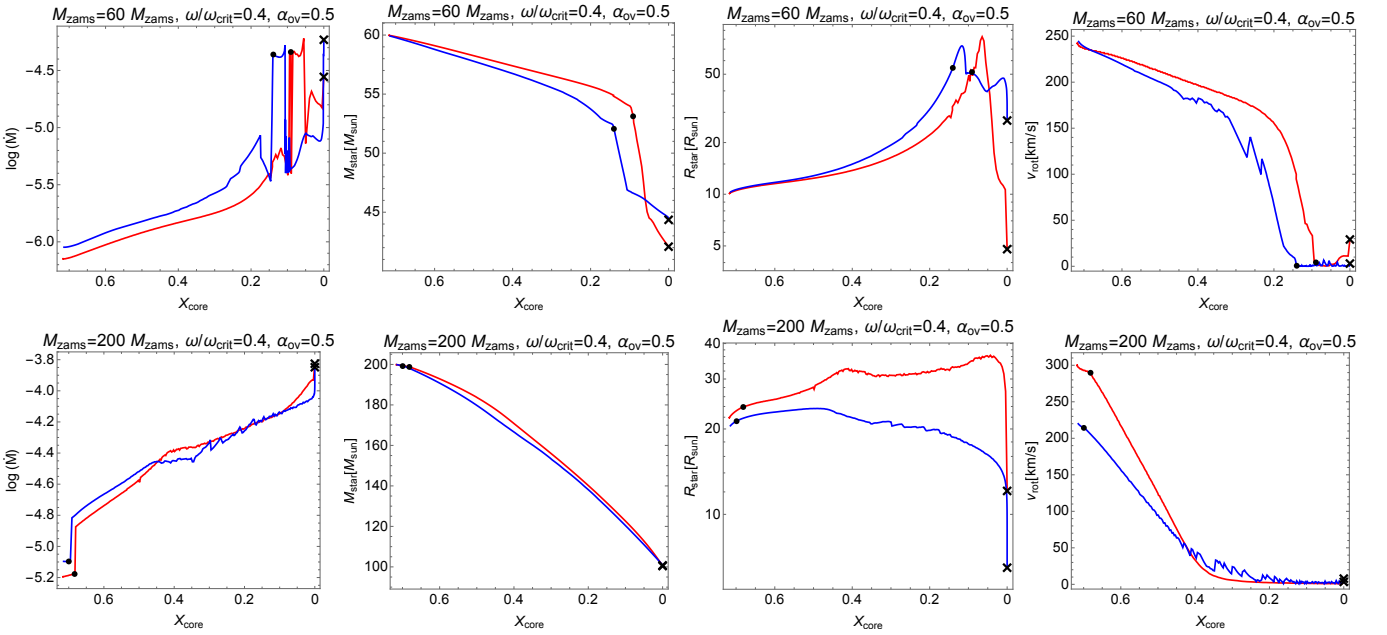


Fig. 2: Left panel: Evolution of mass-loss rate, stellar mass, stellar radius, and Eddington factor during the H-core burning stage for GENEC and MESA evolution models with $M_{\text{zams}} = 60 M_{\odot}$. Right panel: same, but for evolution models with $M_{\text{zams}} = 200 M_{\odot}$.

from Eq. 10, making a difference of ~ 0.2 dex in logarithmic scale. However, for our $M_{\text{zams}} = 60 M_{\odot}$ models, this difference is not large enough to produce significant deviations at the beginning, and thus both tracks move upwards increasing luminosity at temperature nearly constant. Both models reach $\Gamma_e = 0.5$ prior of reaching their maximum radial expansion in the MS, but our GENEC model reaches a higher temperature because of its slightly slower mass loss, its faster rotation, and a more efficient mixing. This is evidenced in Table 1, where the MESA model reaches to the switch point from thin to thick winds (black dots in Figures 1, and 2) with lower mass and lower mass fractions of helium and nitrogen, in contrast with the GENEC model. Once the winds for both models become optically thick, the mass loss in both cases is described either by Eq. 6 or V01/GH08 formulae depending on the condition of T_{eff} being higher or lower than 30 kK. Because our GENEC model has a larger luminosity and larger Γ_e , its optically thick \dot{M} will be larger enough to remove more layers and therefore to end the H-core burning stage with less mass than our MESA model ($42.1 M_{\odot}$ vs $45 M_{\odot}$). However, the most remarkable difference is the final chemical composition at the H-depletion: our GENEC model ends with a helium mass fraction of $Y = 0.929$, i.e., stellar structure is almost homogeneous, and much more compact ($\approx 5 R_{\odot}$) and hotter ($T_{\text{eff}} \approx 90$ kK).

For our $M_{\text{zams}} = 200 M_{\odot}$ models, the initial mass loss start around $10^{-5} M_{\odot} \text{ yr}^{-1}$, and again the MESA model starts with a higher \dot{M} due to Eq. 10. The initial rotational velocity substantially differs between both models, because both models calculate a slightly different starting point for the ZAMS in the HRD as a consequence of the numerical uncertainties (Agrawal et al. 2022b), which tend to increase for larger masses. The initial radius leads to different ω_{crit} according to Eq. 8 and subsequently to different $v_{\text{rot,ini}}$ following the condition $\omega/\omega_{\text{crit}} = 0.4$ from Eq. 9. Despite these minor corrections, both models reach $\Gamma_e = 0.5$ at the very beginning of their lives and subsequently the stars spend more than their 90% of their H-core burning lifetime in the optically thick wind regime. Nonetheless, in this mass regime the mass-loss escalates with metallicity only as $\dot{M} \propto Z^{0.48}$ (according to Eq. 6) and thus our initial mass loss for the thick wind regime is around $\log \dot{M} \approx -4.8$, not large enough to produce an abrupt decrease in the luminosity, reason why both tracks keep moving upwards in the HRD diagram until $\log L/L_{\odot} \approx 6.7$. Once the mass loss increases enough to stop the rise in luminosity, both models move bluewards keeping L_* almost constant. This time, the MESA model drops its rotational velocity slower than the GENEC model, keeping a more moderate radius and ending their H-core burning stage with a larger effective temperature (~ 100 kK, against the ~ 80 kK from the GENEC model). Despite that our GENEC expanded more redwards, it ends its H-burning with a more advanced chemical enrichment at the surface. Even though this could be partially attributed to the larger initial rotation, it is also because that GENEC implements a more efficient rotational mixing (Meynet & Maeder 2000; Choi et al. 2016).

The correlation between the both tracks shows the most important difference with respect to previous evolution studies adopting V01, where it is found that for $M_{\text{zams}} = 200 M_{\odot}$ the mass loss starts being strong enough to make the star quickly drop in luminosity (Yusof et al. 2013; Sabhahit et al. 2022, 2023; Martinet et al. 2023). Differences in mass loss also carries another important discrepancy with respect previous studies: our models end the H-core burning stage with final masses of $\sim 100.5 M_{\odot}$. This is larger than the $M_{\text{final}} \approx 85 M_{\odot}$ found by Martinet et al. (2023) for $M_{\text{zams}} = 180 M_{\odot}$, which is the study with the structure setup closest to ours ($\alpha_{\text{ov}} = 0.2$ and Ledoux

convection criterion) but still adopting old winds; but our result is even more remarkably larger than the $M_{\text{final}} \approx 40 M_{\odot}$ found by Sabhahit et al. (2022, 2023), who adopted a M_{thick} from Vink et al. (2011). In contrast with these huge mass loss, our models adopting weaker (thin and thick) winds makes a $M_{\text{zams}} = 200 M_{\odot}$ star lose ‘only’ one half of their mass at the end of H-core burning stage. This carries an important impact related to the spectroscopic diagnostics to be done over Galactic VMS, as we will see in Sec.4.1.

3.2. He-core and C-core burning stages

Given that the star $60 M_{\odot}$ from our MESA model ends the MS with a less homogeneous chemical structure (only a $\sim 57\%$ of helium mass fraction, in contrast with the $\sim 93\%$ predicted by GENEC), it quickly expands until reaching $T_{\text{eff}} \approx 8000$ K with a maximum radius of $\approx 740 R_{\odot}$. This is because stars keeping a more constant chemical composition from the core to the surface remain in the bluer part of the HR diagram (Maeder 1987). The beginning of the He-core burning stage (black star symbol in the Figures) makes the star return bluewards, thus increasing its temperature and its mass loss. On the contrary, GENEC model predicts a compact star which enters into the He-core burning stage without any radial expansion. This divergence on the models indicate that $M_{\text{zams}} \approx 60 M_{\text{odot}}$ represents a threshold for the Hertzsprung-gap: less massive stars will all expand post MS despite minor differences in the rotational mixing, whereas more massive will not (see Fig. 2 from Romagnolo et al. 2024). These initial differences during He-core ignition later converge into the position at the HRD where both stellar models become H-poor WR stars. Hence, both models show a similar track for the rest of the He-core burning, with a large diminishing in the luminosity from $\log L/L_{\odot} \approx 6.2$ to ≈ 5.75 at temperature almost constant $T_{*} \approx 140$ kK. As a consequence, the final masses at the end of the He-core burning stage are relatively the same for MESA and GENEC tracks ($\approx 16.7 M_{\odot}$), and thus the remaining evolution through the C-core burning is practically identical for both models.

For the $200 M_{\odot}$ case, differences in both the stellar mass and the chemical composition after the H-depletion are almost negligible, and just the HRD where the He-ignition occurs is significantly relevant. Because of its proximity to the Eddington limit (with $\Gamma_e \approx 0.7$) and lower density, the convection at the outer envelope of a star born with $M_{\text{zams}} = 200 M_{\odot}$ is highly superadiabatic (i.e, the temperature gradient is larger than the adiabatic temperature gradient) the thus the energy released in the interior remains locked at the subsurface layers, thus creating numerical instabilities in the models where each evolution code adopts different strategies to handle it (Agrawal et al. 2022a). MESA reduces the superadiabacity in regions by means of the `use_superad_reduction` method, which is more constrained and calibrated than the `MLT++` formalism (Jermyn et al. 2023). On the contrary, our $200 M_{\odot}$ GENEC does not reduce the superadiabacity and the excess in the temperature gradient leads into a considerable expansion of the outer layer in the middle of the He-core burning (Yusof et al. 2013; Martinet et al. 2023), until this excess of energy is released due to Supra-Eddington mass loss (Ekström et al. 2012) and the star returns to its initial radius. During this expansion, only less than the 0.1% of the total mass is inflated, keeping the remaining 99.9% of the total mass constrained into the same stellar radius, reason why this expansion should not be considered for any binary interaction Belczynski et al. (2022). Indeed, we show this expansion due to superadiabatic instability as a sudden expansion redwards in the

HRD of Fig. 1, but we do not consider it for our plot of radial evolution during the He-core burning (Fig. 3) nor for the maximum radius in Table 2. Moreover, the strategies to deal with these superadiabatic instabilities are approached from a numerical point of view, and possibilities of a physical phenomenon have been barely considered. After this phenomenon, the star will decrease its luminosity at almost constant temperature until $\log L/L_{*} \approx 6.0$ according to both MESA and GENEC models, then the He-core burning stage ends with a stellar mass of $\approx 25.5 M_{\odot}$ being the star a ball of $\approx 94\%$ carbon and oxygen. We ultimately reach the end of the C-core burning stage with final masses of $24.4 M_{\odot}$ according to GENEC and $24.8 M_{\odot}$ according to MESA.

4. Observational diagnostics

4.1. Spectroscopic analysis

The new mass-loss prescription, plus the new transition from thin to thick winds, modify the evolutionary tracks across the HR diagram and thus the spectroscopic phases. According to the output of our evolution models, we can classify the spectroscopic phases of our evolution models according to

- O-type: optically thin wind and $T_{\text{eff}} \geq 26.3$ kK.
- B-type: optically thin wind and $T_{\text{eff}} < 26.3$ kK.
- WNL: WR star with $X_{\text{surf}} \geq 0.05$.
- WNE: WR star and $X_{\text{surf}} < 0.05$ and $(^{12}\text{C} + ^{16}\text{O})/^{4}\text{He} \leq 0.03$.
- WC: WR star wind and $(^{12}\text{C} + ^{16}\text{O})/^{4}\text{He} > 0.03$.
- WO: WR star with $\log T_{\text{eff}} \geq 5.25$.

These WR boundaries are derived from the conditions settled by Yusof et al. (2013), Aadland et al. (2022), and Martinet et al. (2023); whereas the distinction between O and B-type is taken from Groh et al. (2014). It is important to note, that this classification is not based on spectral analysis but on the output of our theoretical models, and thus discrepancies may be observed. The results are shown in Table 3.

Even though is not a formal spectroscopic phase, we classify our star as a luminous blue variable (LBV) if the HD-limit ($L > 6 \times 10^5$ and $10^{-5} L^{1/2} R > 1$) is exceeded (Humphreys & Davidson 1994; Hurley et al. 2000). This is particularly evident for our $60 M_{\odot}$ MESA model, where the post MS expansion exceeds the HD limit and therefore the star spends 12 kyr (0.26% of its total lifetime) as a LBV. Despite this short period, the star had a mass of $M_{\text{pre,lbv}} \approx 44.1 M_{\odot}$ and $X_{\text{H}} \approx 0.4$, to finish with $M_{\text{post,lbv}} \approx 41.9 M_{\odot}$ and $X_{\text{H}} \approx 0.24$, i.e., it experienced an average mass loss of $\dot{M}_{\text{lbv}} \approx 1.8 \times 10^{-4} M_{\odot} \text{ yr}^{-1}$ ($\log \dot{M}_{\text{lbv}} \approx -3.7$). Such value is close to the adopted \dot{M}_{lbv} by Belczynski et al. (2010), but still it comes from the application of the wind recipes of Vink et al. (2001) and de Jager et al. (1988) in a region of the HRD beyond the HD limit. Models for eruptive mass loss (Quataert et al. 2016; Cheng et al. 2024), more in agreement with the nature of LBVs, would be more require to better represent the evolution during this phase. In parallel, our $60 M_{\odot}$ GENEC does not become a LBV because its more chemically homogeneous structure avoids any radial expansion after the H-depletion. Therefore, despite that the final masses tabulated for both codes are quite similar, the prediction about the existence or not of the LBV phenomenon strongly depends on the calculated mixing during the main sequence stage.

In opposition, our $200 M_{\odot}$ GENEC evolution track moves redwards, crossing the HD limit, between its phases WNE and WC. This reinforces the uncertain relation of the LBV phenomenon with the evolution of massive stars because, if we consider that

Table 2: Properties of our evolution models during the He-core and C-core burning stages.

Initial parameters		He-core burning									C-core burning						
M_{zams} [M_{\odot}]	code	τ_{He} [Myr]	M_{final} [M_{\odot}]	M_{core} [M_{\odot}]	R_{max} [R_{\odot}]	Y_{surf}	$X(\text{C})_{\text{surf}}$ mass fraction	$X(\text{O})_{\text{surf}}$	Γ_{e}	τ_{C} [Myr]	M_{final} [M_{\odot}]	M_{core} [M_{\odot}]	R_{max} [R_{\odot}]	Y_{surf}	$X(\text{C})_{\text{surf}}$ mass fraction	$X(\text{O})_{\text{surf}}$	Γ_{e}
60	GENEC	4.657	16.7	11.9	7.1	0.059	0.317	0.600	0.497	4.662	16.1	12.6	0.79	0.044	0.286	0.646	0.654
60	MESA	4.546	16.6	16.6	763.0	0.059	0.345	0.578	0.482	4.552	16.1	16.1	0.95	0.047	0.319	0.616	0.589
200	GENEC	2.835	25.4	18.4	12.1	0.032	0.200	0.746	0.596	2.839	24.4	19.2	1.0	0.020	0.171	0.784	0.736
200	MESA	2.855	25.7	25.7	11.6	0.036	0.230	0.714	0.578	2.860	24.8	24.8	1.27	0.026	0.205	0.748	0.668

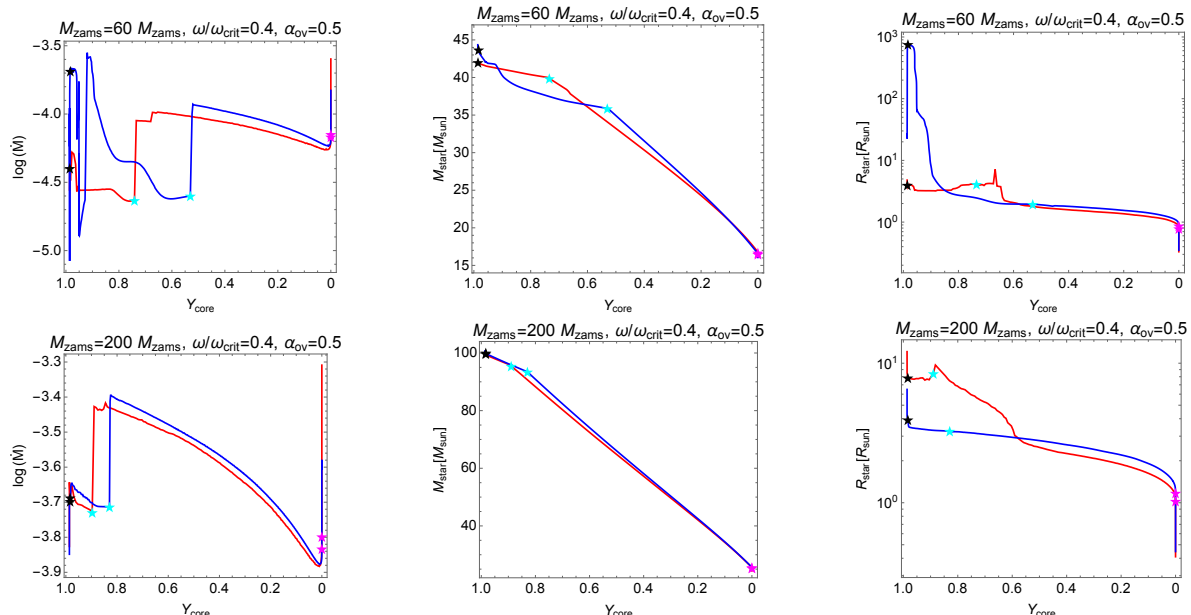


Fig. 3: Left panel: Evolution of mass-loss rate, stellar mass, stellar radius, and Eddington factor during the He-core and C-core burning stages for GENEC and MESA evolution models with $M_{\text{zams}} = 60 M_{\odot}$. Right panel: same, but for evolution models with $M_{\text{zams}} = 200 M_{\odot}$.

Table 3: Lifetime (in Myr) predicted by our GENEC and MESA models in the spectroscopic phases according to stellar evolution. The percentages with respect to the total lifetime are shown in parenthesis.

M_{zams}	code	$\Delta\tau_{\text{O}}$	$\Delta\tau_{\text{B}}$	$\Delta\tau_{\text{WNL}, X_{\text{surf}} > 0.3}$	$\Delta\tau_{\text{LBV}}$	$\Delta\tau_{\text{WNL}, X_{\text{surf}} < 0.3}$	$\Delta\tau_{\text{WNE}}$	$\Delta\tau_{\text{WC}}$	$\Delta\tau_{\text{WO}}$
60	GENEC	3.942 (84.55%)	0.017 (0.38%)	0.205 (4.40%)	0 (0%)	0.141 (3.01%)	0.069 (1.48%)	0.283 (6.08%)	0.005 (0.10%)
60	MESA	3.701 (81.29%)	0.031 (0.67%)	0.461 (10.14%)	0.012 (0.26%)	0.071 (1.57%)	0.061 (1.35%)	0.211 (4.64%)	0.004 (0.08%)
200	GENEC	0.183 (6.45%)	0 (0%)	1.679 (59.14%)	0.006 (0.22%)	0.574 (20.21%)	0.108 (3.79%)	0.285 (10.03%)	0.004 (0.15%)
200	MESA	0.092 (3.21%)	0 (0%)	1.794 (62.72%)	0 (0%)	0.602 (21.04%)	0.096 (3.37%)	0.273 (9.55%)	0.003 (0.11%)

redwards expansion as a physical phenomenon instead of a numerical artefact, it would mean that LBV events can occur even after the star becomes a hydrogen depleted WN star (something not found observationally). Besides the standard classification for WR stars, in Table 3 we also separate the WNL stars with $X_{\text{H}} > 0.3$. Given that typical stellar evolution models enter into the WR phase when either $X_{\text{H}} < 0.3$ (Ekström et al. 2012) or $X_{\text{H}} < 0.4$ (Brott et al. 2011), this distinction is made to incorporate the WNL stars whose optically thick winds are because of the proximity to the Eddington limit before the H-depletion, according to the criterion $\Gamma_{\text{e}} \geq 0.5$ established in Sec. 2.2.1. Thus we discern from the WNL stars which are result of the ‘classical’ evolution, where the star becomes a WR due to the drift bluewards after the LBV episodes during the He-core burning stage (Conti 1975; Groh et al. 2014). Indeed, WNL stars with $X_{\text{H}} \geq 0.3$ are constrained to a very narrow band of temperature in the HRD, $\log T_{\text{eff}} \approx 4.5 - 4.62$ (Martins et al. 2008; Crowther et al. 2010), whereas WNL stars with $X_{\text{H}} \leq 0.3$ are spread across a wider range of temperatures (Martins 2023). To illustrate better this point, we select the Galactic WNL stars (with $X_{\text{H}} \geq 0.3$) from the Arches cluster (Martins et al. 2008), from

the NGC 3603 cluster (Crowther et al. 2010), and from the local neighbourhood (Hamann et al. 2019), and we tabulated them in Table 4. In addition, we plot our GENEC and MESA models for 60 and 200 M_{\odot} , highlighting the segments where $\Gamma_{\text{e}} \geq 0.5$ and $X_{\text{H}} \geq 0.3$. The results are shown in Fig. 4. Despite the limited differences between the evolution tracks, our prescription adequately describes the narrow band where WNL exist, thus meaning that WNL are the product of stars born with $M_{\text{zams}} \geq 60 M_{\odot}$ which produce optically thick winds before the H-depletion due to their proximity to the Eddington limit. In the middle we append models for 100 M_{\odot} , showing that the thick band also fits the WNL of our sample.

For the 200 M_{\odot} cases the observational diagnostics are more uncertain. For instance, the stars tabulated in Table 4 are also the brightest WNL stars in the Milky Way, and none of them reaches the luminosity of $\log L_{\ast} / \log L_{\odot} \gtrsim 6.55$. The early approaching to the Eddington limit from the very beginning of the main sequence implies that the O-type phase in our models is very short, and therefore the star will spend the largest percentage of their lifetime (almost a $\sim 90\%$ for both models) as a WNL. This is a remarkable difference with respect to previous studies, where

Table 4: WNh stars included in Fig. 4.

Star	Sp. Type	T_*	L_*	X_{H}	Ref.
		[kK]	$[L_{\odot}]$	mass frac.	
B1	WN8-9h	32.2	5.95	0.70	1
F1	WN8-9h	33.7	6.30	0.70	1
F2	WN8-9h	34.5	6.0	0.41	1
F4	WN8-9h	37.3	6.3	0.38	1
F7	WN8-9h	33.7	6.30	0.45	1
F9	WN8-9h	36.8	6.35	0.70	1
F12	WN8-9h	37.3	6.20	0.55	1
F14	WN8-9h	34.5	6.00	0.70	1
F16	WN8-9h	32.4	5.90	0.70	1
A1a	WN6h	42.0	6.39	0.60	2
A1b	WN6h	40.0	6.18	0.70	2
B	WN6h	42.0	6.46	0.60	2
C	WN6h	44.0	6.35	0.70	2
WR 24	WN6ha-w	50.1	6.47	0.44	3
WR 87	WN7h	44.7	6.21	0.40	3

References. (1) Martins et al. (2008); (2) Crowther et al. (2010); (3) Hamann et al. (2019).

very massive stars still spent the majority of their lifetime as O-type stars until they remove more than the half of their initial surface H abundance (Martinet et al. 2023). In other words, our models predict that extremely luminous Galactic stars have more probabilities of being WNh than O-type. The star W49-#2, with $\log L_*/L_{\odot} \approx 6.64 \pm 0.25$ (one of the brightest stars known in the Milky Way) is classified as O2-3.5If* (Wu et al. 2016) but quite close of being a Of/WN star based on the spectral classification of Crowther & Walborn (2011). In any case, the high stellar mass ($\sim 250 M_{\odot}$) estimated by Wu et al. (2016) implies $\Gamma_e \approx 0.35-0.46$ (depending on the X_{H} to be considered in Eq. 3), thus not being close to the Eddington limit enough to develop optically thick winds.

Beyond WNh stars, our new evolution models for 200 M_{\odot} also predicts the existence of H-poor WN stars with extremely high luminosities, whereas only two WN (WR 18 and WR 37) stars with $X_{\text{H}} = 0$ satisfies $\log L_*/L_{\odot} > 6.0$ in the Galactic catalog of Hamann et al. (2019). Same for WC type, WR 126 is the only WN/WC star with $\log L_*/L_{\odot} > 6.0$ in the Milky Way (Sander et al. 2019). However, we need to emphasise that stars born with 200 M_{\odot} are very rare, ~ 17 times less abundant than stars with $M_{\text{zams}} = 60 M_{\odot}$ according to the IMF from Salpeter (1955), and our current stellar Galactic catalogs are quite constrained to our solar neighbourhood. The study and discoveries of new sources at the edge of the known stellar luminosities, together with less uncertain data, is beyond of the scope of this work.

4.2. Self-consistent mass loss close to $\Gamma_{e,trans}$

The transition from thin to thick winds based on the proximity of the Eddington factor, has been recently studied by Gräfenner (2021) and Sabhahit et al. (2023), where the switch from OB to WNh stars is set by using the relationship between the optical depth at the sonic point of the wind structure (τ_s) and the wind efficiency number ($\eta \equiv \dot{M}v_{\infty}/(L_*/c)$) from Gräfenner et al. (2017)

$$\tau_s \approx \frac{\dot{M}v_{\infty}}{L_*/c} \left(1 + \frac{v_{\text{esc}}^2}{v_{\infty}^2} \right), \quad (12)$$

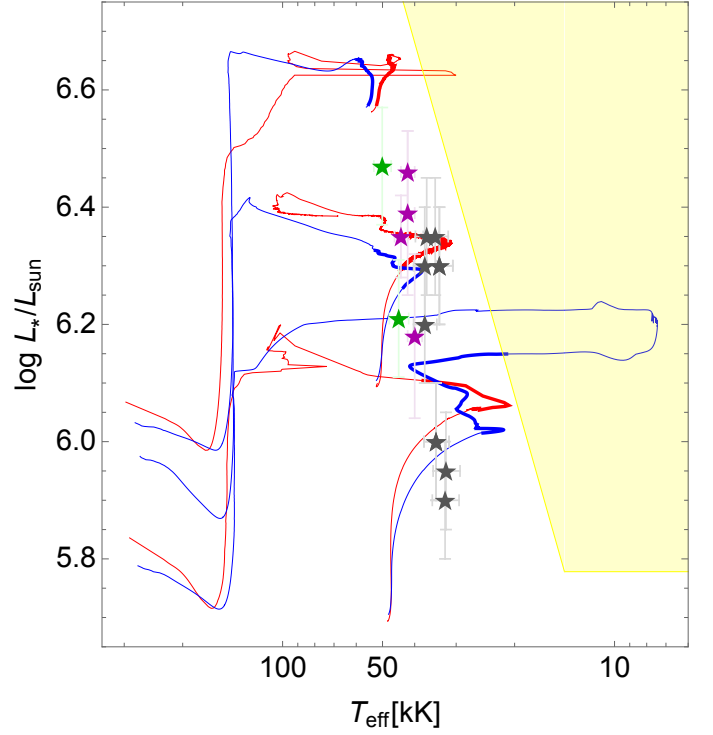


Fig. 4: Evolutionary GENEC and MESA tracks for 60 and 200 M_{\odot} from Fig.1 and additional 100 M_{\odot} models, where the thick solid lines represent the segments where the wind is optically thick ($\Gamma_e \geq 0.5$) and $X_{\text{surf}} \geq 0.3$. The gray stars correspond to the sample of WNh stars from Martins et al. (2008), the purple stars to the sample of Crowther et al. (2010) and the green stars to the sample of Hamann et al. (2019), tabulated in Table 4. Yellow shadowed area correspond to the HRD region where the HD limit is exceeded.

with v_{∞} and v_{esc} being the wind terminal and the escape velocities respectively.

Since η denotes the ratio between the mechanical wind momentum and the total momentum of the radiatively-driven wind, the value $\eta = 1$ corresponds to the single scattering limit. If $\eta \geq 1$, it means that photons can be absorbed and re-emitted through the wind structure more than once (Lucy & Abbott 1993). Consequently, Eq. 12 implies that the transition to thick winds will be given when $\tau_s \geq 1$, thus meaning that the sonic point of the wind structure is located below the photosphere (at $\tau_R = 2/3$). This approach however, still adopts \dot{M}_{V01} for the optically thin regime even for cases $M_{\text{zams}} \approx 40 - 60 M_{\odot}$ (Sabhahit et al. 2022, 2023), and thus it does not consider the new recipes for mass-loss rate (Krtićka & Kubát 2017; Björklund et al. 2021; Gormaz-Matamala et al. 2022b).

Therefore, a question that arises it is how the transition works if we consider self-consistent mass-loss rates for the optically thin regime (low Γ_e). To do so, we plot in Fig.5 the \dot{M}_{sc} as a function of the Eddington factor coming from the models introduced in Gormaz-Matamala et al. (2023), plus the GENEC models introduced in this work. We can see that the $\dot{M} - \Gamma_e$ easily correlates with a linear fit in the log-log plane, as

$$\log \dot{M}_{\text{sc}} \approx -4.547 + 2.709 \log \Gamma_e, \quad (13)$$

Which agrees reasonably well with the $\dot{M} \propto \Gamma_e^{2.73 \pm 0.43}$ from Bestenlehner et al. (2014) and with the $\dot{M} \propto \Gamma_e^{2.69}$ from (Brands et al. 2022), for the low Eddington factor regime. In other words, Eq. 4 behaves like Eq. 6 when $\Gamma_e \lesssim 0.5$. The only difference will be the jump in the resulting value for the mass-loss rate, which

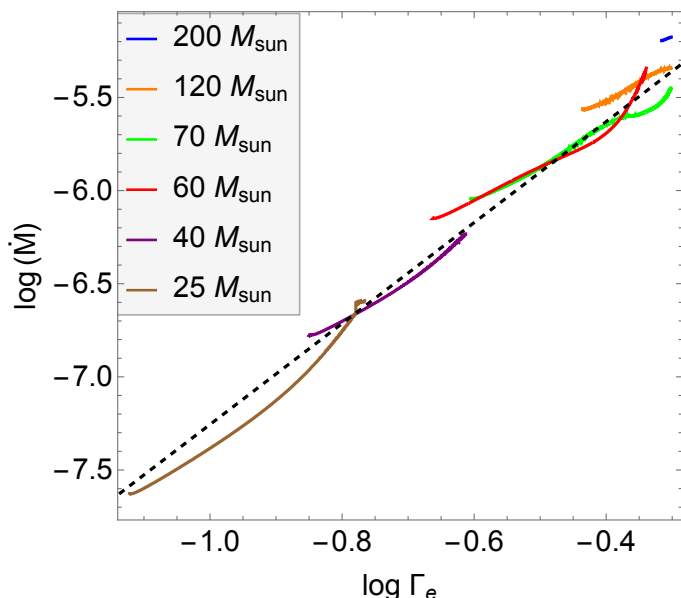


Fig. 5: $\dot{M} - \Gamma_e$ correlations taken from the GENEC self-consistent evolution models from Gormaz-Matamala et al. (2023) and this work. The dashed line represents the best linear fit.

is the same jump in \dot{M} in ~ 0.5 dex that we observe in the Fig. 2. It is important to mention that even though the $\dot{M} - \Gamma_e$ correlation is a very useful tool to describe the escalation of the mass loss in the proximity of the Eddington limit, it is not a formal function. The value of \dot{M} may vary for a same value of Γ_e , if the stellar mass or the luminosity or the hydrogen abundance are different. In particular, the linear behaviour of \dot{M}_{sc} dissipates as we approach $\Gamma_e \approx 0.5$, thus suggesting that the m-CAK prescription (which assumes single scattering for the line-driven) stops being valid for regimes with larger Eddington factor (where multi-scattering effects on the line-driven mechanism becomes more dominant) and a prescription considering optically thick winds needs to be adopted.

As seen in Fig. A7 from Gormaz-Matamala et al. (2023), Eddington factor increases as the star evolves in time, with weaker winds boosting that tendency. The more massive the star, the faster it reaches $\Gamma_{e,trans} = 0.5$ and therefore the shortest its fraction of MS lifetime adopting \dot{M}_{sc} . In the case of the evolution models introduced in this work, a $60 M_\odot$ star will spend $\sim 92\%$ of its MS lifetime exhibiting optically thick winds ($\sim 92\%$ for the MESA model), in contrast with the $\sim 7\%$ of the MS lifetime for a $200 M_\odot$ star ($\sim 4\%$ for the MESA model). Therefore, the chosen stellar masses for the analysis in this work represent the approximated limits where optically thin and thick winds can coexist during the main sequence stage. For stars with $M_{zams} < 60 M_\odot$ the limit $\Gamma_e = 0.5$ may not be reached during the MS and therefore the stars will just become classical WR after the depletion of hydrogen, as in traditional evolution models. On the other limit, for stars with $M_{zams} \geq 200 M_\odot$ it is satisfied that $\Gamma_e = 0.5$ from the ZAMS and therefore the wind is fully optically thick, as also found by Sabhahit et al. (2023). In the intermediate mass range, stars will spend one fraction of their lifetime with thin OB-type winds and reduced mass-loss as reported by Gräfener (2021), and the other fraction with the enhanced \dot{M} if WNh stars. Summarising, the new weaker winds from Gormaz-Matamala et al. (2022b, 2023) can be applied for all initial masses for the earliest stages, even for VMS, for the segment of time when $\Gamma_e < 0.5$ is satisfied.

5. Summary and conclusions

In Paper I (Romagnolo et al. 2024) we explored the expected final masses prior to the core collapse, when we calculate stellar evolution updating the mass-loss prescription. In this work, we confirm the importance of these new wind prescriptions, by analysing its impact over the expected spectroscopic stages (OB-type, WNh and classical WR).

Regardless of the unification of the overshooting ($\alpha_{ov} = 0.5$), the rotation ($\omega/\omega_{crit} = 0.4$), the angular momentum transport (Tayler-Spruit dynamo), the convective boundary criterion (Ledoux), and the line-driven mass-loss prescriptions for both codes GENEC and MESA, there are important differences between the calculated evolutionary tracks. For instance, GENEC computes a more prominent rotational mixing during the main sequence phase, leading to a more homogeneous stellar structure at the H-core depletion in comparison with MESA. This is particularly evident for our $60 M_\odot$ models, where our less homogeneous model largely expands and crosses the HD limit before the He-ignition. Such discrepancy between both models can be interpreted as a boundary in the mass range below which stars normally expands, and over which stars keep a moderate size because of the strong outflows (Romagnolo et al. 2023). For the $200 M_\odot$ models, due to the large size of the convective core the differences between both evolution codes are less relevant, and only the treatment for the superadiabacity during the H-core burning phase is a matter of debate.

Concerning stellar masses, both GENEC and MESA codes show similar results at the end of each core burning process, with the most remarkable mass losses during the post-MS stages. Models with $M_{zams} = 60 M_\odot$ end the H-core burning with final masses of 42.1 and $44.5 M_\odot$ respectively, subsequently experiencing strong outflows during He-core burning stages to finish with $16.1 M_\odot$ at the C-core depletion. This is a striking discrepancy with the $M_{bh} \approx 30 M_\odot$ found at $M_{zams} = 60 M_\odot$ by Bavera et al. (2023), where the rotational effects were not considered. For our $200 M_\odot$ case, where the main sequence is almost fully dominated by thick winds, both GENEC and MESA models predict a final mass of $\sim 100 M_\odot$ at the end of the H-core burning stage, finishing later with $M_{fin} \approx 24.6 M_\odot$ at the C-core depletion. This result is also largely discrepant with other studies such as Yusof et al. (2013) or Sabhahit et al. (2022, 2023), who found that a star with $M_{zams} = 200 M_\odot$ would loss almost the $\sim 80\%$ of its mass during the H-burning stage only. Despite the discussion introduced in Section 4.2, such difference is not produced for the approach of the transition from thin to thick winds close to the Eddington factor, but due to the lower recipes for \dot{M} for both thin –(Gormaz-Matamala et al. 2023) instead of V01– and thick –Bestenlehner (2020) instead of Vink et al. (2011)– wind regimes.

However, the most remarkable result is that our transition between the optically thin winds of OB-type stars and the thick winds of WNh stars based on the proximity to the Eddington limit, results in the prediction of a band in the HRD where stars are expected to develop optically thick winds but with large hydrogen fractions at the surface ($X_{surf} \gg 0.3$). This band corresponds to effective temperatures between $\log T_{eff} \approx 4.5 - 4.62$, in agreement with the spectroscopic diagnostics of Martins et al. (2008), Crowther et al. (2010), and Hamann et al. (2019).

The basis for our switch of wind regime at $\Gamma_{e,trans} = 0.5$ follows the formulation of Bestenlehner (2020) based on CAK theory, and it adequately considers that at early evolutionary stages the \dot{M} for regular massive stars (i.e., not VMS) is ~ 3 times lower than the traditionally assumed for V01. This statement is compatible with the idea of having WNh stars born

from $M_{\text{zams}} \approx 60 M_{\odot}$, whereas we find reduced \dot{M} from hydrodynamic analysis on winds for the same mass range (Sander et al. 2017; Gormaz-Matamala et al. 2021). As we escalate in the mass range, the fraction of MS time at which the stellar wind is optically thin becomes shorter, and therefore the wind of very massive stars posses enhanced values of mass-loss rates because they spent larger fractions of their MS dominated by thick winds. Stars at $M_{\text{zams}} \gtrsim 200 M_{\odot}$ are already dominated by thick winds from the very beginning, as found by Sabhahit et al. (2023).

This work focuses on calculations applicable to stars with solar metallicity and in earlier stages of evolution. However, recent observations reveal a significant population of Wolf-Rayet stars (WNh) in young and metal-poor clusters like R136 (Brands et al. 2022) and 30 Dor Ramírez-Agudelo et al. (2017), both located in the LMC. This necessitates extending our procedures and diagnostics to encompass very massive stars with metallicities as low as $Z \lesssim 0.006$, as suggested by Martins & Palacios (2022). Additionally, these upgrades in mass-loss prescriptions need to be applicable to stars with $T_{\text{eff}} \leq 30$ kK. Evaluating approaches like those proposed by Krtićka et al. (2024) for B-supergiants is a promising avenue for future work.

Acknowledgements. Authors acknowledge support from the Polish National Science Center grant Maestro (2018/30/A/ST9/00050). The authors also thank the GENEC and MESA communities at large for their helpful feedback on the models creation. Computations for this article have been performed using the computer cluster at CAMK PAN. ACGM thanks the support from project 10108195 MERIT (MSCA-COFUND Horizon Europe). We dedicate this paper to Krzysztof Belczyński, who contributed to this research before his untimely passing on 13th January 2024.

References

- Aadland, E., Massey, P., Hillier, D. J., et al. 2022, *ApJ*, 931, 157
 Abbott, B. P., Abbott, R., Abbott, T. D., et al. 2016, *Phys. Rev. Lett.*, 116, 061102
 Abbott, D. C. 1982, *ApJ*, 259, 282
 Abbott, R., Abbott, T. D., Abraham, S., et al. 2021, *ApJ*, 913, L7
 Agrawal, P., Hurley, J., Stevenson, S., Szécsi, D., & Flynn, C. 2020, *MNRAS*, 497, 4549
 Agrawal, P., Stevenson, S., Szécsi, D., & Hurley, J. 2022a, *A&A*, 668, A90
 Agrawal, P., Szécsi, D., Stevenson, S., Eldridge, J. J., & Hurley, J. 2022b, *MNRAS*, 512, 5717
 Araya, I., Curé, M., ud-Doula, A., Santillán, A., & Cidale, L. 2018, *MNRAS*, 477, 755
 Asplund, M., Grevesse, N., Sauval, A. J., & Scott, P. 2009, *ARA&A*, 47, 481
 Baraffe, I., Clarke, J., Morison, A., et al. 2023, *MNRAS*, 519, 5333
 Bavera, S. S., Fragos, T., Zapartas, E., et al. 2023, *Nature Astronomy*, 7, 1090
 Belczyński, K., Bulik, T., Fryer, C. L., et al. 2010, *ApJ*, 714, 1217
 Belczyński, K., Hirschi, R., Kaiser, E. A., et al. 2020a, *ApJ*, 890, 113
 Belczyński, K., Klencki, J., Fields, C. E., et al. 2020b, *A&A*, 636, A104
 Belczyński, K., Romagnolo, A., Olejak, A., et al. 2022, *ApJ*, 925, 69
 Bestenlehner, J. M. 2020, *MNRAS*, 493, 3938
 Bestenlehner, J. M., Gräfener, G., Vink, J. S., et al. 2014, *A&A*, 570, A38
 Björklund, R., Sundqvist, J. O., Puls, J., & Najarro, F. 2021, *A&A*, 648, A36
 Björklund, R., Sundqvist, J. O., Singh, S. M., Puls, J., & Najarro, F. 2023, *A&A*, 676, A109
 Bouret, J. C., Lanz, T., & Hillier, D. J. 2005, *A&A*, 438, 301
 Brands, S. A., de Koter, A., Bestenlehner, J. M., et al. 2022, *A&A*, 663, A36
 Brott, I., de Mink, S. E., Cantiello, M., et al. 2011, *A&A*, 530, A115
 Castor, J. I., Abbott, D. C., & Klein, R. I. 1975, *ApJ*, 195, 157
 Cheng, S. J., Goldberg, J. A., Cantiello, M., et al. 2024, *arXiv e-prints*, arXiv:2405.12274
 Choi, J., Dotter, A., Conroy, C., et al. 2016, *ApJ*, 823, 102
 Conti, P. S. 1975, *Memoires of the Societe Royale des Sciences de Liege*, 9, 193
 Crowther, P. A. 2007, *ARA&A*, 45, 177
 Crowther, P. A., Schnurr, O., Hirschi, R., et al. 2010, *MNRAS*, 408, 731
 Crowther, P. A. & Walborn, N. R. 2011, *MNRAS*, 416, 1311
 Curé, M. 2004, *ApJ*, 614, 929
 Curé, M. & Rial, D. F. 2004, *A&A*, 428, 545
 de Jager, C., Nieuwenhuijzen, H., & van der Hucht, K. A. 1988, *A&AS*, 72, 259
 Eggenberger, P., Ekström, S., Georgy, C., et al. 2021, *A&A*, 652, A137
 Eggenberger, P., Meynet, G., Maeder, A., et al. 2008, *Ap&SS*, 316, 43
 Ekström, S., Georgy, C., Eggenberger, P., et al. 2012, *A&A*, 537, A146
 Ekström, S., Meynet, G., Maeder, A., & Barblan, F. 2008, *A&A*, 478, 467
 Farrell, E., Groh, J. H., Hirschi, R., et al. 2021, *MNRAS*, 502, L40
 Fryer, C. L., Olejak, A., & Belczyński, K. 2022, *ApJ*, 931, 94
 Gaia Collaboration, Panuzzo, P., Mazeh, T., et al. 2024, *arXiv e-prints*, arXiv:2404.10486
 Georgy, C., Meynet, G., & Maeder, A. 2011, *A&A*, 527, A52
 Georgy, C., Saio, H., & Meynet, G. 2014, *MNRAS*, 439, L6
 Gormaz-Matamala, A. C., Cuadra, J., Ekström, S., et al. 2024, *arXiv e-prints*, arXiv:2404.07570
 Gormaz-Matamala, A. C., Cuadra, J., Meynet, G., & Curé, M. 2023, *A&A*, 673, A109
 Gormaz-Matamala, A. C., Curé, M., Cidale, L. S., & Venero, R. O. J. 2019, *ApJ*, 873, 131
 Gormaz-Matamala, A. C., Curé, M., Hillier, D. J., et al. 2021, *ApJ*, 920, 64
 Gormaz-Matamala, A. C., Curé, M., Lobel, A., et al. 2022a, *A&A*, 661, A51
 Gormaz-Matamala, A. C., Curé, M., Meynet, G., et al. 2022b, *A&A*, 665, A133
 Gräfener, G. 2021, *A&A*, 647, A13
 Gräfener, G. & Hamann, W. R. 2008, *A&A*, 482, 945
 Gräfener, G., Owocki, S. P., Grassitelli, L., & Langer, N. 2017, *A&A*, 608, A34
 Gräfener, G., Owocki, S. P., & Vink, J. S. 2012, *A&A*, 538, A40
 Gräfener, G., Vink, J. S., de Koter, A., & Langer, N. 2011, *A&A*, 535, A56
 Groh, J. H., Meynet, G., Ekström, S., & Georgy, C. 2014, *A&A*, 564, A30
 Hamann, W. R., Gräfener, G., Liermann, A., et al. 2019, *A&A*, 625, A57
 Hawcroft, C., Mahy, L., Sana, H., et al. 2024, *arXiv e-prints*, arXiv:2407.06775
 Hawcroft, C., Sana, H., Mahy, L., et al. 2021, *A&A*, 655, A67
 Heger, A., Fryer, C. L., Woosley, S. E., Langer, N., & Hartmann, D. H. 2003, *ApJ*, 591, 288
 Heger, A., Woosley, S. E., & Spruit, H. C. 2005, *ApJ*, 626, 350
 Higgins, E. R., Sander, A. A. C., Vink, J. S., & Hirschi, R. 2021, *MNRAS*, 505, 4874
 Huang, W., Gies, D. R., & McSwain, M. V. 2010, *ApJ*, 722, 605
 Humphreys, R. M. & Davidson, K. 1994, *PASP*, 106, 1025
 Humphreys, R. M., Weis, K., Davidson, K., & Gordon, M. S. 2016, *ApJ*, 825, 64
 Hurley, J. R., Pols, O. R., & Tout, C. A. 2000, *MNRAS*, 315, 543
 Ishii, M., Ueno, M., & Kato, M. 1999, *PASJ*, 51, 417
 Ivanova, N., Justham, S., Chen, X., et al. 2013, *A&A Rev.*, 21, 59
 Jermyn, A. S., Bauer, E. B., Schwab, J., et al. 2023, *ApJS*, 265, 15
 Josiek, J., Ekström, S., & Sander, A. A. C. 2024, *arXiv e-prints*, arXiv:2404.14488
 Köhler, K., Langer, N., de Koter, A., et al. 2015, *A&A*, 573, A71
 Krtićka, J. & Kubát, J. 2017, *A&A*, 606, A31
 Krtićka, J. & Kubát, J. 2018, *A&A*, 612, A20
 Krtićka, J., Kubát, J., & Krtićková, I. 2024, *A&A*, 681, A29
 Langer, N. 1998, *A&A*, 329, 551
 Ledoux, P. 1947, *ApJ*, 105, 305
 Lucy, L. B. & Abbott, D. C. 1993, *ApJ*, 405, 738
 Lucy, L. B. & Solomon, P. M. 1970, *ApJ*, 159, 879
 Maeder, A. 1987, *A&A*, 178, 159
 Maeder, A. & Meynet, G. 2000, *A&A*, 361, 159
 Martinet, S., Meynet, G., Ekström, S., Georgy, C., & Hirschi, R. 2023, *arXiv e-prints*, arXiv:2309.00062
 Martinet, S., Meynet, G., Ekström, S., et al. 2021, *A&A*, 648, A126
 Martins, F. 2023, *A&A*, 680, A22
 Martins, F., Hillier, D. J., Paumard, T., et al. 2008, *A&A*, 478, 219
 Martins, F. & Palacios, A. 2022, *A&A*, 659, A163
 Meynet, G. & Maeder, A. 2000, *A&A*, 361, 101
 Meynet, G. & Maeder, A. 2005, *A&A*, 429, 581
 Meynet, G., Maeder, A., Schaller, G., Schaerer, D., & Charbonnel, C. 1994, *A&AS*, 103, 97
 Muijres, L. E., de Koter, A., Vink, J. S., et al. 2011, *A&A*, 526, A32
 Olejak, A., Belczyński, K., & Ivanova, N. 2021, *A&A*, 651, A100
 Olejak, A., Fryer, C. L., Belczyński, K., & Baibhav, V. 2022, *MNRAS*, 516, 2252
 Pauli, D., Oskinova, L. M., Hamann, W. R., et al. 2022, *A&A*, 659, A9
 Paxton, B., Bildsten, L., Dotter, A., et al. 2011, *ApJS*, 192, 3
 Paxton, B., Cantiello, M., Arras, P., et al. 2013, *ApJS*, 208, 4
 Paxton, B., Marchant, P., Schwab, J., et al. 2015, *ApJS*, 220, 15
 Paxton, B., Schwab, J., Bauer, E. B., et al. 2018, *ApJS*, 234, 34
 Paxton, B., Smolec, R., Schwab, J., et al. 2019, *ApJS*, 243, 10
 Petrovic, J., Pols, O., & Langer, N. 2006, *A&A*, 450, 219
 Puls, J., Vink, J. S., & Najarro, F. 2008, *Astronomy and Astrophysics Review*, 16, 209
 Quataert, E., Fernández, R., Kasen, D., Klion, H., & Paxton, B. 2016, *MNRAS*, 458, 1214
 Ramírez-Agudelo, O. H., Sana, H., de Koter, A., et al. 2017, *A&A*, 600, A81
 Romagnolo, A., Belczyński, K., Klencki, J., et al. 2023, *MNRAS*, 525, 706
 Romagnolo, A., Gormaz-Matamala, A. C., & Belczyński, K. 2024, *ApJ*, 964, L23
 Sabhahit, G. N., Vink, J. S., Higgins, E. R., & Sander, A. A. C. 2022, *MNRAS*, 514, 3736

- Sablahit, G. N., Vink, J. S., Sander, A. A. C., & Higgins, E. R. 2023, MNRAS, 524, 1529
- Salpeter, E. E. 1955, ApJ, 121, 161
- Sander, A. A. C., Hamann, W.-R., Todt, H., Hainich, R., & Shenar, T. 2017, A&A, 603, A86
- Sander, A. A. C., Hamann, W. R., Todt, H., et al. 2019, A&A, 621, A92
- Sander, A. A. C., Lefever, R. R., Poniatowski, L. G., et al. 2023, A&A, 670, A83
- Sander, A. A. C. & Vink, J. S. 2020, MNRAS, 499, 873
- Sander, A. A. C., Vink, J. S., & Hamann, W. R. 2020, MNRAS, 491, 4406
- Scott, L. J. A., Hirschi, R., Georgy, C., et al. 2021, MNRAS, 503, 4208
- Sibony, Y., Georgy, C., Ekström, S., & Meynet, G. 2023, A&A, 680, A101
- Spruit, H. C. 2002, A&A, 381, 923
- Sundqvist, J. O., Björklund, R., Puls, J., & Najarro, F. 2019, A&A, 632, A126
- Tayler, R. J. 1973, MNRAS, 161, 365
- Tehrani, K. A., Crowther, P. A., Bestenlehner, J. M., et al. 2019, MNRAS, 484, 2692
- Venero, R. O. J., Curé, M., Puls, J., et al. 2024, MNRAS, 527, 93
- Vink, J. S. 2017, A&A, 607, L8
- Vink, J. S. 2021, arXiv e-prints, arXiv:2109.08164
- Vink, J. S., de Koter, A., & Lamers, H. J. G. L. M. 2001, A&A, 369, 574
- Vink, J. S. & Gräfener, G. 2012, ApJ, 751, L34
- Vink, J. S., Higgins, E. R., Sander, A. A. C., & Sablahit, G. N. 2021, MNRAS, 504, 146
- Vink, J. S., Muijres, L. E., Anthonisse, B., et al. 2011, A&A, 531, A132
- Šurlan, B., Hamann, W. R., Aret, A., et al. 2013, A&A, 559, A130
- Wu, S.-W., Bik, A., Bestenlehner, J. M., et al. 2016, A&A, 589, A16
- Yusof, N., Hirschi, R., Meynet, G., et al. 2013, MNRAS, 433, 1114

Appendix A: Effects of TS dynamo for angular momentum transport

For our GENEC models, we include Tayler-Spruit dynamo (Tayler 1973; Spruit 2002; Heger et al. 2005) for the treatment of the angular momentum transport, besides adopting Ledoux instead of Schwarzschild criterion for the treatment of convective layers (Martinet et al. 2023). The evolution during the MS phase is basically not affected by differences in convection treatment, and just for the H-core burning the Ledoux criterion improves the agreement between models and observations for the surface abundances of BSGs evolving back from RSGs (Georgy et al. 2014). For stars with $M_{\text{zams}} \geq 60 M_{\odot}$ (as in this study), the impact of the different convective criterion is almost negligible because mass loss become the main driver of the evolution (Sibony et al. 2023).

In Fig. A.1 we show the evolution tracks of our models shown in Section 3, compared to models with the same input but adopting the original inner structure of GENEC. The initial rotation this time follows the framework $\Omega = v/v_{\text{crit}} = 0.4$ (equivalent to $\omega/\omega_{\text{crit}} \approx 0.58$, see Eq. 9). The evolution of the rotational speed during the main sequence is shown in Fig. A.2, whereas the final parameters between both cases are displayed in Table A.1.

As expected, the differences between adopting the new or the old inner structure are minimal, and are reduced to braking in the stellar rotation since the ZAMS to the TAMS. TS dynamo produces a more efficient transport of angular momentum from the core to the surface, and therefore the stellar surface will rotate faster than in the case without TS. This impact is stronger for the 60 M_{\odot} and almost negligible for the 200 M_{\odot} models, because of the larger convective core of VMS.

Regardless of the HRD tracks, TS dynamo actually affects the stellar inner structure. Fig. A.3 shows how the specific angular momentum $j_r = \omega_r R^2$ at the end of the He-core burning stage is more depleted when TS dynamo is incorporated, due to the more efficient angular momentum transport. Again, the influence is more prominent for the case with the smaller convective core. Even though, adoption of TS dynamo have an impact on the expected spin of the resulting black hole (Belczynski et al. 2020b), for the analysis of the evolution of stars with $M_{\text{zams}} \geq 60 M_{\odot}$ its impact is not relevant enough.

Table A.1: Table of final parameters for our GENEC evolution models, comparing new inner structure (Tayler-Spruit dynamo and Ledoux convective criterion) with old inner structure (no-TS dynamo and Schwarzschild convective criterion).

Initial parameters		End of H-core burning						End of He-core burning						End of C-core burning					
M_{zams}	inn struct	M_{tot}	M_{core}	R_{max}	τ_{H}	Y_{surf}	Γ_{e}	M_{tot}	M_{core}	R_{max}	τ_{He}	Y_{surf}	Γ_{e}	M_{tot}	M_{core}	R_{max}	τ_{C}	Y_{surf}	Γ_{e}
$[M_{\odot}]$		$[M_{\odot}]$	$[M_{\odot}]$	$[R_{\odot}]$	[Myr]			$[M_{\odot}]$	$[M_{\odot}]$	$[R_{\odot}]$	[Myr]			$[M_{\odot}]$	$[M_{\odot}]$	$[R_{\odot}]$	[Myr]		
60	TS dyn, Led	44.8	37.6	44.8	4.425	0.853	0.599	17.3	12.2	7.3	4.784	0.051	0.508	16.7	12.6	0.84	4.789	0.037	0.675
60	mer cur, Sch	48.1	40.2	18.9	4.507	0.974	0.572	16.5	11.5	16.1	4.880	0.052	0.488	15.9	12.6	0.81	4.885	0.037	0.656
200	TS dyn, Led	100.2	87.9	38.2	2.525	0.972	0.691	25.5	18.3	10.4	2.841	0.034	0.594	24.4	19.2	1.1	2.845	0.023	0.733
200	mer cur, Sch	106.2	94.5	42.1	2.569	0.976	0.698	25.6	18.7	9.9	2.886	0.034	0.592	24.6	19.4	1.1	2.890	0.023	0.739

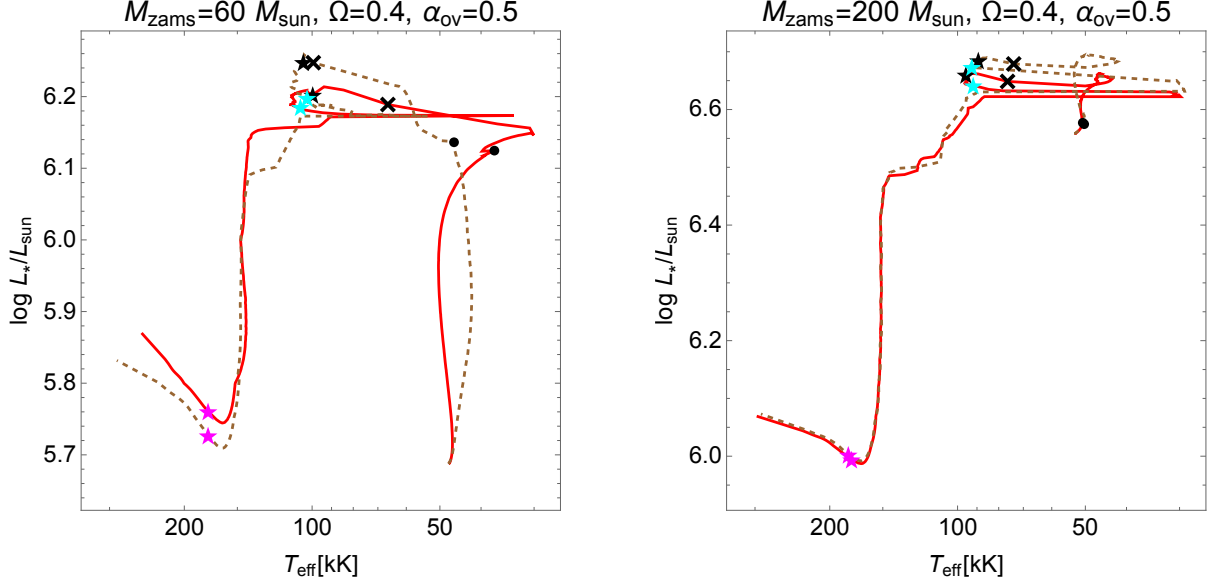


Fig. A.1: HR diagram for our GENEC evolution models, comparing new inner structure (Tayler-Spruit dynamo and Ledoux convective criterion, red solid lines) with old inner structure (no-TS dynamo and Schwarzschild convective criterion, dashed brown lines).

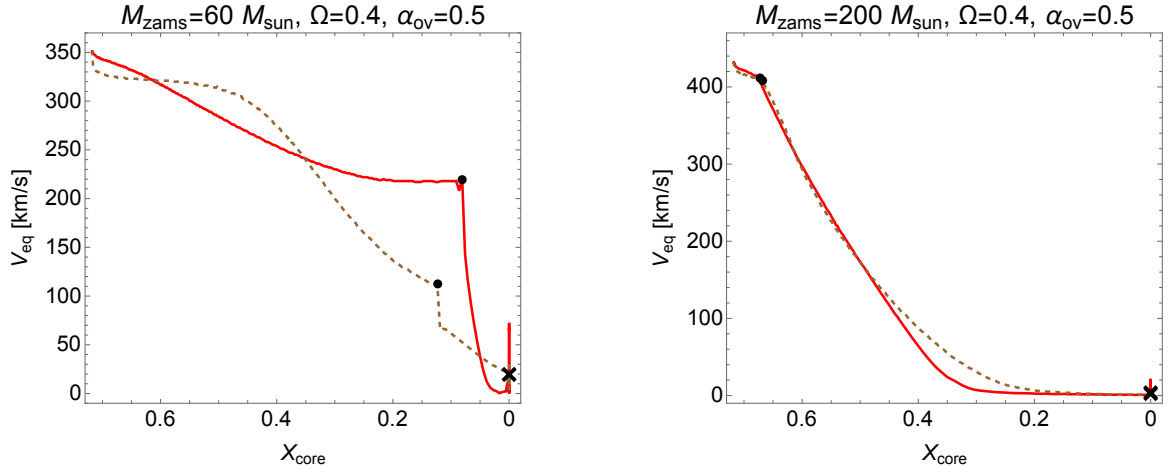


Fig. A.2: Rotational velocity during the MS for our GENEC evolution models, comparing new inner structure (Tayler-Spruit dynamo and Ledoux convective criterion, red solid lines) with old inner structure (no-TS dynamo and Schwarzschild convective criterion, dashed brown lines).

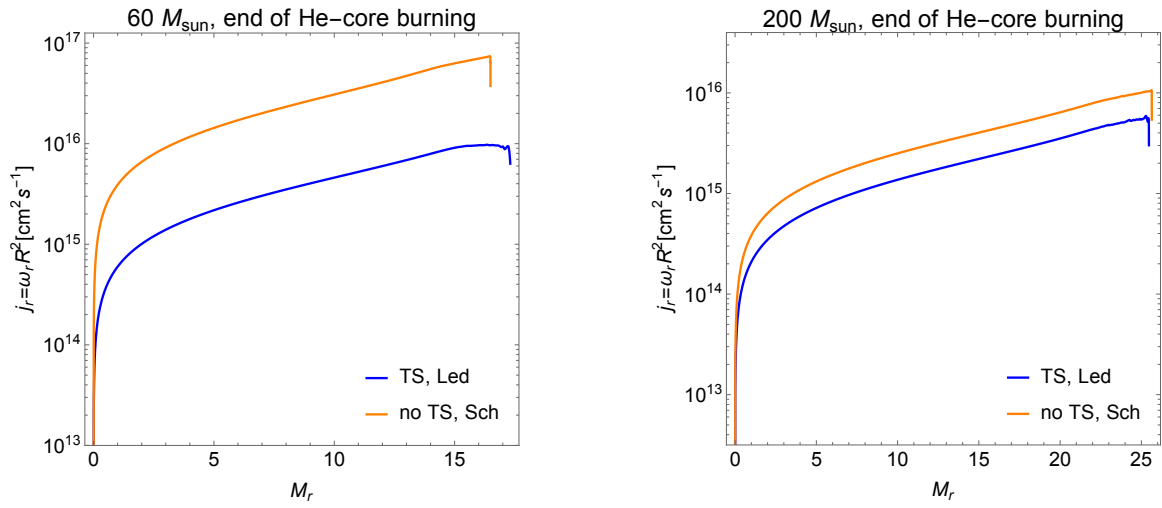


Fig. A.3: Specific angular momentum at the end of the He-core burning for our GENEC evolution models, comparing new inner structure (Tayler-Spruit dynamo and Ledoux convective criterion, blue) with old inner structure (no-TS dynamo and Schwarzschild convective criterion, orange).